RESEARCH ARTICLE

**ADVANCED
INTELLIGENT
SYSTEMS**
Open Access

www.advintellsyst.com

Topology Optimization of Exo-Glove Poly II for Enhancing Functionality and Wearability

Soomin Choi, Kyu Bum Kim, Donguk Kwon, Brian Byunghyun Kang,*
and Kyu-Jin Cho*

This study presents a novel design method for the finger body of Exo-Glove Poly II (EGP II) that enhances functionality and wearability by minimizing distortion and achieving user-preferred stretchability. Minimizing distortion restores the intended flexion moment arms at the finger joints, ensuring target functionality. User-preferred stretchability minimizes constraints on the user's finger flexion, improving wearability. To satisfy these conflicting goals, the finger body as a longitudinally periodic structure and develop a corresponding unit cell-level optimization is developed. Specifically, finger body-level evaluations are converted into equivalent unit cell-level analyses. A novel metric, distortional compliance—defined as a weighted sum of unit cell-level compliances—is introduced as the optimization objective. To account for large deformation effects, a two-step optimization approach is employed: topology optimization under a linear elastic assumption, followed by size optimization considering material and geometric nonlinearities. Experimental validation considers three users with different hand sizes. Results show that the optimized designs reduce distortion by 54.9% on average compared to the previous version, while achieving target stretchability within a 4.43% error. The optimized EGP II exhibits minimal distortion, increased grasping force (15.3% on average), and user-preferred wearability, thereby demonstrating the effectiveness of the proposed method.

S. Choi, D. Kwon
School of Mechanical Engineering
Kyungpook National University
Daegu 41566, South Korea

K. B. Kim, K.-J. Cho
Department of Mechanical Engineering
Seoul National University
Seoul 08826, South Korea
E-mail: kjcho@snu.ac.kr

B. B. Kang
Department of Artificial Intelligence and Robotics
Sejong University
Seoul 05006, South Korea
E-mail: brianbkang@sejong.ac.kr

1. Introduction

In tendon-driven soft wearable robots,[1,2] the wearable components consist of a tendon routing system for power transmission and deformable bodies made of elastomers or fabrics. Remote actuation by the tendon-driven mechanism makes the wearable components compact and lightweight. Bioinspired routings allow these components to operate more effectively. Accordingly, these features enable the robots to assist users with weakened or paralyzed muscles during activities of daily living (e.g., for upper limbs[3–12] and lower limbs[13–22]). Moreover, recent studies have improved the usability of such robots,[3,23–28] including their wearability.[29–32]

Leveraging the aforementioned advantages of tendon-driven soft wearable robots, Exo-Glove Poly II[33] (EGP II, **Figure 1**a) was developed to assist the flexion and extension of the index and middle fingers of individuals with spinal cord injuries. In the wearable components, the finger body has a diamond-shaped pattern, which allow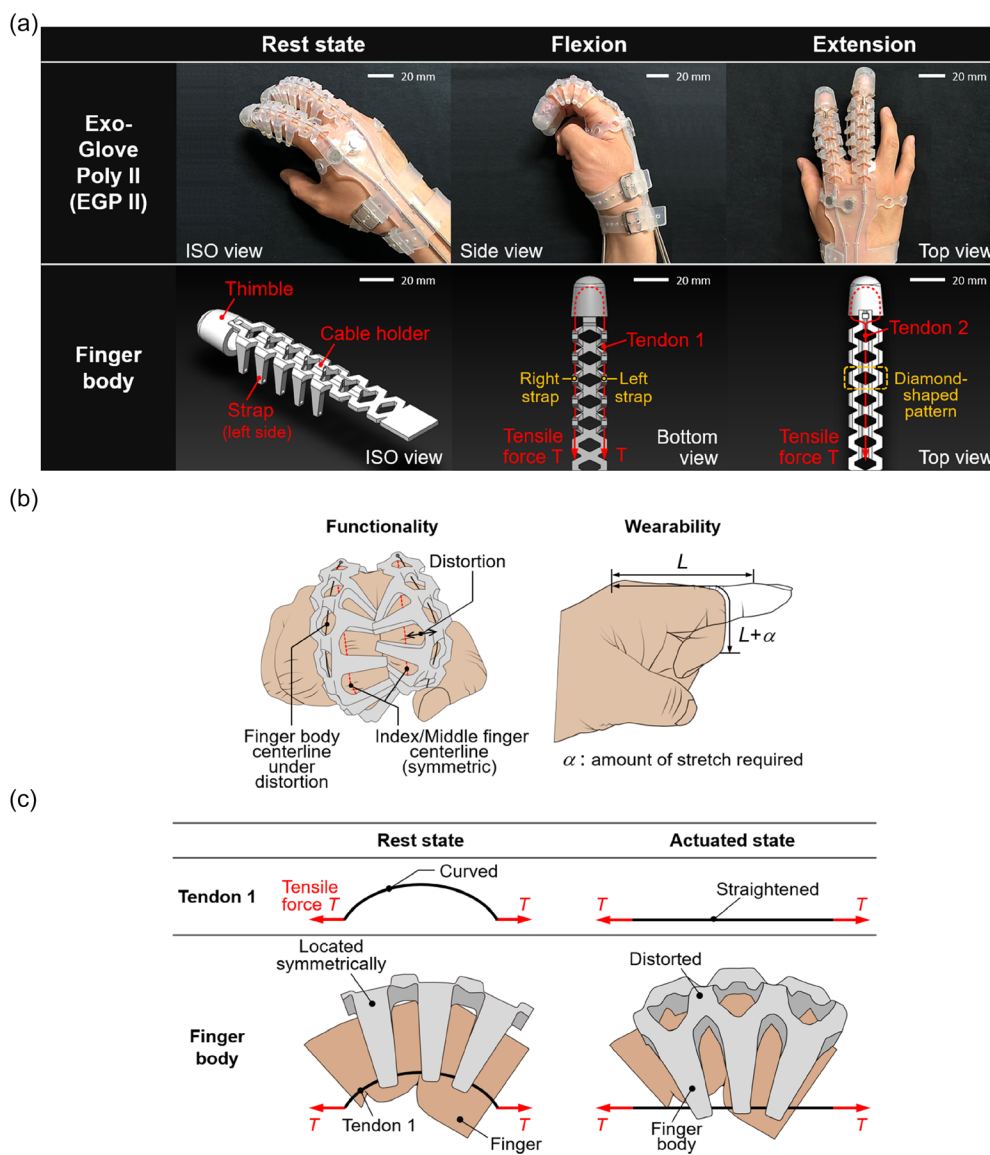s it to easily stretch during flexion and be adapted for users with different hand sizes. The flexion of the index and middle fingers is induced by a single tendon (Tendon 1) passing through straps, where the straps determine the length of the flexion moment arm for each finger joint. The extension is induced by two separate tendons (Tendon 2) passing through cable holders. The effective design of the tendon routing system enables EGP II to adaptively grasp objects of different shapes and sizes through an under-actuation mechanism. Subsequent studies have also improved EGP II's usability, including grasping force estimation,[34] user intention detection,[35] and durability.[36]

Nevertheless, EGP II faces a design issue: the finger body exhibits undesirable distortional deformation when assisting flexion (Figure 1b). The primary cause of this issue appears to be asymmetric external loads induced by friction. Specifically, Tendon 1, which bends during flexion, tends to straighten under the applied tensile force T (Figure 1c), thereby exerting external loads on the finger body in the direction normal to its path. Here, the magnitudes of the external loads exerted by the left and right straps differ due to friction between Tendon 1 and the teflon tube inside the thimble,[1,16,37] and this asymmetry causes distortion

Figure 1. a) EGP II and its finger body. b) Design requirements for the finger body: i) minimizing distortion to help EGP II attain its target functionality and ii) meeting the target stretchability for flexion to provide the user-desired wearability. c) Illustration explaining why distortion occurs in the finger body.

in the finger body. The resulting distortion alters the intended length of the flexion moment arm, thereby compromising the EGP II's functionality. Moreover, it causes repeated actuation in an unstable posture and generates shear forces on the skin that lead to discomfort,[16,38] thus reducing the EGP II's wearability.

To prevent distortion, one may choose materials with as high a stiffness as possible, as suggested in the design guidelines[16] of the Harvard exosuit. However, this approach restricts the user's kinematics during flexion, reducing the wearability of EGP II. To enhance the stretchability of the finger body while preventing distortion, linear elastic metamaterials,[39–42] which selectively lower specific elastic moduli, can be employed; however, these metamaterials should consist of numerous meta-atoms that are much smaller than the finger body, raising the level of

difficulty in manufacturing. Alternatives include mechanism-based metamaterials,[43–47] which can realize large amounts of strain, auxetic material behavior, multistability, and shape changes through origami and kirigami. However, these materials require widely spread flexible hinges, which may result in an undesirable reduction in distortional stiffness. Recent studies[48,49] have proposed synthetic metamaterials composed of programmable organohydrogels with multistable mechanical states, offering the ability to alter mechanical stiffness. However, the lack of understanding regarding which type of stiffness in the finger body plays a critical role in reducing distortion makes it difficult to utilize these approaches effectively.

From these backgrounds, we propose a new finger body design method for EGP II that can minimize distortion while providing the desired stretchability for flexion. To this end, we

assume the finger body to be a patterned structure with periodicity along the longitudinal direction (Section 2) and then find an optimal pattern design to replace the existing diamond pattern. This approach allows us to define the design domain as a single-periodic unit cell rather than the entire finger body. It also enables the evaluation of distortional stiffness and stretchability for flexion using the same design domain; without the aforementioned periodicity, the distortional stiffness and stretchability need to be evaluated using respective finger bodies with different shapes (Section 3), which would hinder the sharing of the same design domain for optimization. However, for the proposed approach to be feasible, unit cell-level evaluations equivalent to the finger body-level evaluations in Section 3 should be derived, and the detailed derivations are presented in Section 4.

The obtained unit cell-level evaluations enable the unit cell design optimization. To find the optimal unit cell pattern, we conduct topology optimization,[50–52] which, unlike other techniques, requires no preliminary design. Additionally, it facilitates solving optimization problems with conflicting requirements, which are difficult to solve by the designer's intuition and experience. Section 5 introduces a method of defining a distortional compliance as a weighted sum of compliances corresponding to the unit cell-level evaluations. This method enables the formulation of a topology optimization problem that minimizes distortional compliance, thereby yielding an optimal unit cell design with maximum distortional stiffness.

The stretchability for flexion is formulated as a constraint in the optimization problem. Specifically, we establish a sample-based preference test (Section 3) to determine the user's preferred finger body stretchability. Based on subjective feedback, we derive the target tensile compliance for the unit cell and define the target compliance as an equality constraint in the optimization problem. This approach, together with the determination of the finger body dimensions tailored to the user, enables a custom design of the EGP II finger body.

Consequently, we formulate an optimization problem that minimizes the distortional compliance while meeting the stretchability constraint. Topology optimization is then conducted to find a solution satisfying the conflicting requirements. However, topology optimization encounters a convergence issue[50] when material and geometric nonlinearities are incorporated into the unit cell-level evaluations, although these nonlinearities should be taken into account to meet the design requirements of EGP II under large deformations. To address this issue, topology optimization is first performed under a linear elastic assumption (Section 6). Subsequently, using the topology optimization result as a preliminary design, size optimization is carried out (Section 7). Since material and geometric nonlinearities are incorporated into size optimization, this two-step optimization approach enables the derivation of an optimal solution that satisfies the design requirements under large deformations.

The proposed design method is employed to solve three optimization problems, considering three users with different hand sizes. The resulting finger bodies are evaluated via the finger body-level tests and simulations (Section 8). In addition, we evaluate how the optimized finger body improves EGP II's distortion prevention capability and wearability when assisting the user's flexion.

2. Finger Body and Periodic Unit Cell

The EGP II finger body was designed with a generous length and diamond pattern to accommodate users having various hand sizes. However, this versatility renders the finger body prone to distortion, which highlights the need for a custom design to enhance the distortional stiffness.

In response to this need, we define the finger body dimensions based on the user's finger dimensions (**Figure 2**). Additionally, as mentioned in Section 1, we assume the finger body to be a patterned structure with longitudinal periodicity and define the design domain as a single-periodic unit cell (Figure 2), the pattern of which will be derived through optimization.
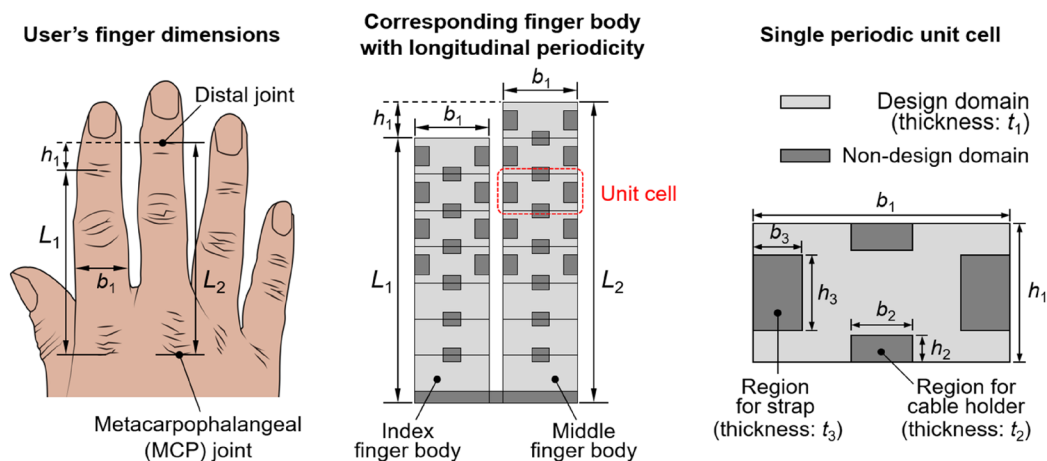
Figure 2. Dimensions of the finger body and its periodic unit cell. For a custom design to enhance the distortional stiffness, the dimensions $\{L_1, L_2, b_1, b_2, b_3, h_1, h_2, h_3, t_1, t_2, t_3\}$ are defined based on the user's finger dimensions (Section 2) and fixed during optimization. In the finger body, the regions for the straps and cable holders (i.e., dark gray regions) are designated as the nondesign domain, which is completely filled with material and does not change during optimization, to maintain EGP II's functionality. Hence, we find the optimal material layout for the given design domain (light gray regions) through the proposed optimization.

**ADVANCED
SCIENCE NEWS**

www.advancedsciencenews.com

**ADVANCED
INTELLIGENT
SYSTEMS**
Open Access

www.advintellsyst.com

The finger body width b_1 is set to the maximum width of the index and middle fingers. The finger body length L_i ($i = 1, 2$) is set to the distance between the metacarpophalangeal joint and the distal joint. The unit cell length h_1 is set to the difference between L_1 and L_2.

If L_i ($i = 1, 2$) is not divisible by h_1, the remainder is placed at the lower end of the finger body and defined as a nondesign domain (the nondesign domain refers to a region that is completely filled with material and does not change during optimization) (Figure 2). The regions for the straps and cable holders are also designated as the nondesign domain to maintain the EGP II's functionality.

The other dimensions (i.e., $\{b_2, b_3, h_2, h_3, t_1, t_2, t_3\}$) are less relevant to the user's finger dimensions and are defined based on the EGP II's previous design with a diamond pattern.[33]

$$b_2 = b_2^{\text{pre}}, \quad b_3 = b_3^{\text{pre}}, \quad h_2 = h_2^{\text{pre}}, \quad h_3 = (h_1/h_1^{\text{pre}}) \cdot h_3^{\text{pre}},$$
$$t_1 = t_1^{\text{pre}}, \quad t_2 = t_2^{\text{pre}}, \quad t_3 = b_1 - 1 \quad (\text{unit} : \text{mm}) \tag{1}$$

where the superscript preindicates the dimensions of the EGP II's previous design.

3. Finger Body-Level Evaluations

This section establishes finger body-level tests and simulations that evaluate distortional stiffness and stretchability. These tests and simulations enable us to evaluate how the optimized finger body improves distortion prevention and wearability. The finger body-level simulations also allow us to derive equivalent unit cell-level simulations, enabling the optimization of the unit cell design.

3.1. Experimental Tests

Figure 3a depicts the finger body-level test setups. The stretchability test is designed to evaluate the wearability of a finger body design based on the following equation.

$$P \approx P^* \quad (P^* : \text{Target force}) \tag{2}$$

Here, P denotes the force required to extend the finger body by an amount α, which corresponds to the elongation during flexion (Figure 1b). This force is measured using the Instron 5948 Micro Tester. To ensure a stringent design criterion, the index finger body—requiring a greater degree of material stretch due to its higher α/L_1 ratio compared to α/L_2—is considered in the evaluation.

In Equation (2), P^* represents the user-selected target force, which is determined through the sample-based preference test (Figure 3b) consisting of the following steps:

Step 1: Measure the user's finger dimensions (Figure 2) and determine the corresponding α.

Step 2: Provide finger body samples tailored to the measured dimensions (Figure 3b). All samples share the same rectangular pattern (the rectangular pattern refers to a unit cell configuration in which the entire design domain is fully filled with solid material, without any internal voids or structural features) but vary in thickness t_1, ranging from 0.5 to 1.25 mm.

Step 3: The user wears each sample and selects the one that offers the most comfortable fit during flexion.

Step 4: The tensile force required to extend the selected sample by α is measured using the Instron 5948 Micro Tester. This value is defined as the target force P^*.

Accordingly, Equation (2) implies that a finger body design can be considered to offer user-desired wearability if the measured force P is approximately equal to the user-determined target force P^*.

The distortion test has a setup that approximates the situation in Figure 1c. The user's finger (or bone) is represented by a finger-shaped rigid structure having a solid circular cross-section with radius r ($= b_1/2 - b_3$, Figure 3c) and a quarter-arc profile with arc length L_2. Since the middle finger body—which has a lower distortional stiffness due to $L_2 > L_1$—is considered here, the design requirement is again more stringent. To impose an asymmetric load, a tensile force $T = T^*$ is applied to Tendon 1, which passes through the straps on the right.

The distortion test measures the maximum β occurring under T^*, where β, indicating the distortion, is defined as the x-directional displacement of the cable holder (Figure 3c). To this end, the β_M value of marker 1 is first measured using the V120: Trio (Optitrack) and the 5948 Micro Tester. Then, we calculate β based on the following relation, which holds for the geometry shown in Figure 3c.

$$\beta_M : \{r + t_1 + (t_2 - t_1) + d\} = \beta : \{r + t_1 + \tfrac{t_2 - t_1}{2}\} \tag{3}$$

The value of T^* is set to match the force T that causes significant distortion (i.e., $\beta = 2r/3$) in the finger body of the previous design (Figure 1a).

Accordingly, the test allows us to evaluate the distortional stiffness of the finger body and define the design requirement for distortion prevention as minimization of β.
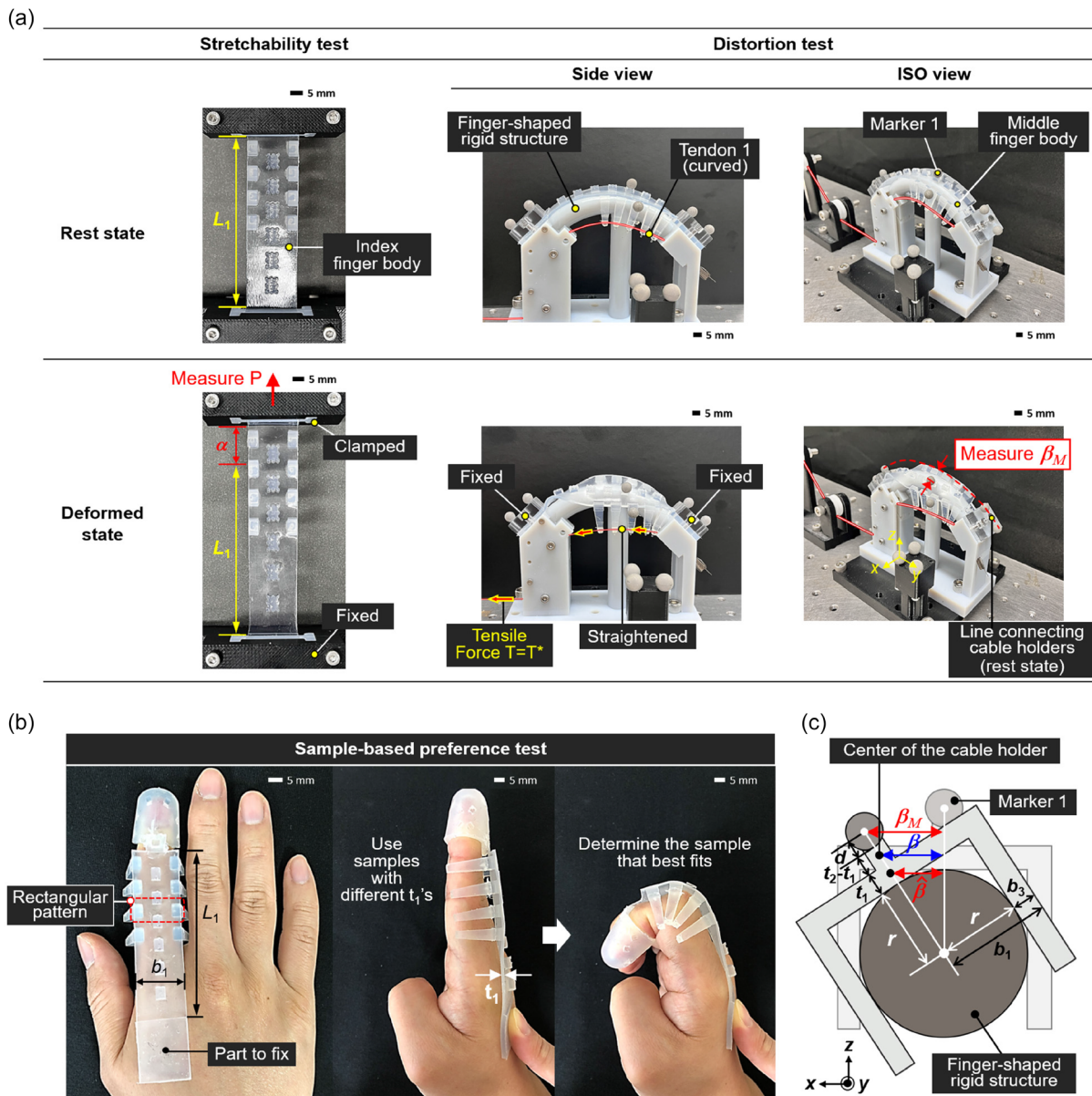
3.2. Numerical Simulations

Figure 4a illustrates two Abaqus[53] numerical simulations corresponding to the tests shown in Figure 3a. To capture the nonlinear behavior of the finger body, the simulations incorporate geometric nonlinearity by employing a geometrically nonlinear finite element analysis and material nonlinearity by adopting the Yeoh model[54] as a hyperelastic material model. Additionally, the contact effect of the user's finger is taken into account by imposing displacement constraints in the thickness direction on the left straps. Further details on the simulation modeling, including the treatment of these nonlinearities, are provided below.

The stretchability analysis is performed using S4R (4-node shell element with reduced integration)—a typical shell element in Abaqus—to model the finger body, the thickness t_1 of which is lower than its other dimensions. To approximate the material volumes of the cable holders and straps, the stretchability analysis introduces their effective thicknesses $\{t_2^e, t_3^e\}$, which satisfy the following conditions

$$t_2^e \times (b_2 \times h_2) = V_{\text{CH}}, \quad t_3^e \times (b_3 \times h_3) = V_{\text{Strap}} \tag{4}$$

where V_{CH} and V_{Strap} represent the actual volumes of the cable holder and strap, respectively (Figure 1). To induce uniform extension at all top edge points (clamped boundary condition

**ADVANCED
SCIENCE NEWS**
www.advancedsciencenews.com

**ADVANCED
INTELLIGENT
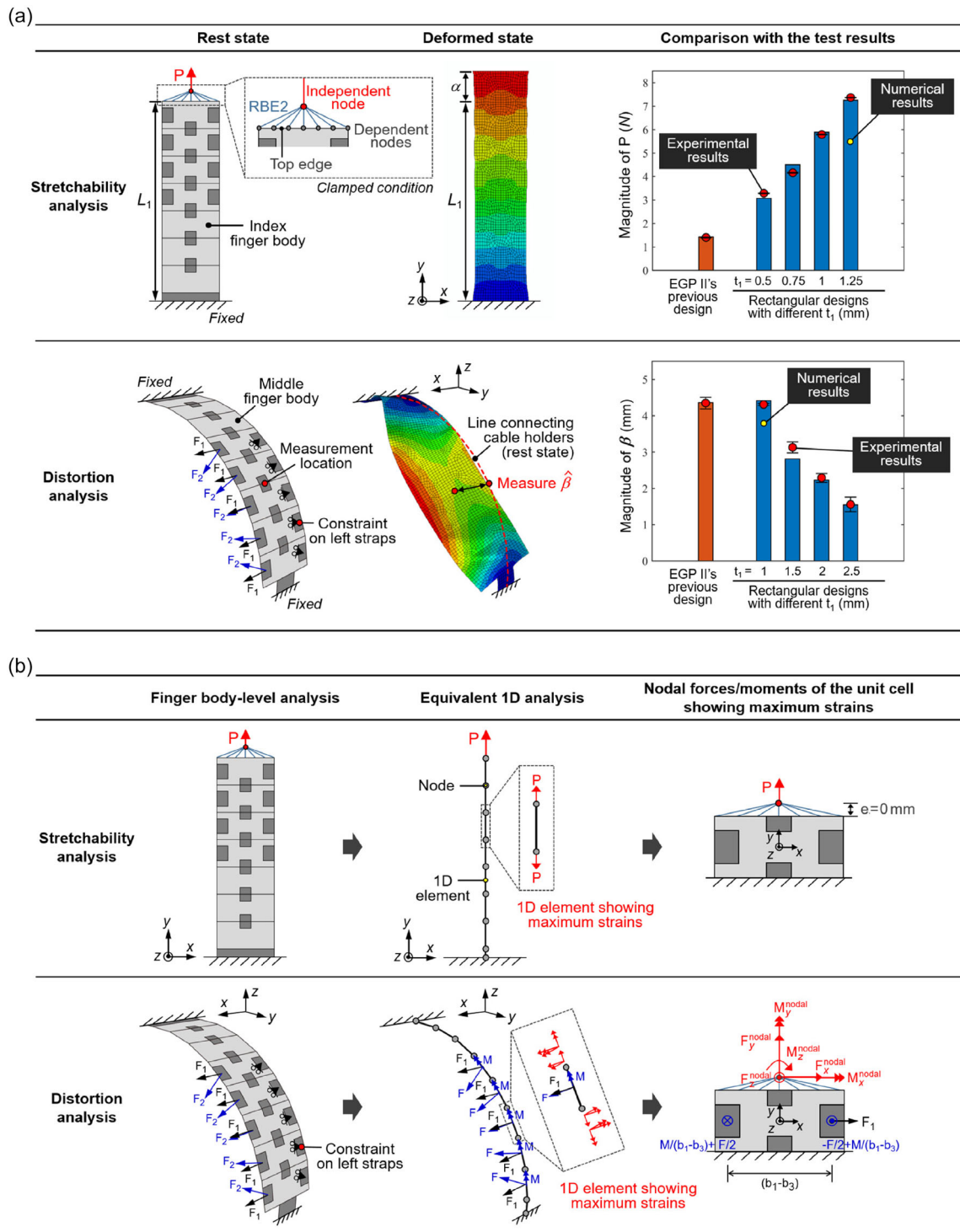SYSTEMS**
Open Access
www.advintellsyst.com

Figure 3. a) Finger body-level tests to evaluate distortional stiffness and stretchability. b) Sample-based preference test to determine the user-selected target force P^*. c) Relationship between $\{\beta, \beta_M, \hat{\beta}\}$, which represent the x-directional displacements measured at the centroids of the cable holder, Marker 1, and the unit cell design domain, respectively.

in Figure 3a), we employ rigid body element type 2 (RBE2), a typical rigid body element in Abaqus. RBE2 rigidly connects dependent nodes to an independent node, preventing any relative displacement along the top edge. The Yeoh model, with material constants $\{C_{10}, C_{20}, C_{30}\}$, is employed as the hyperelastic material model to capture the nonlinear responses of the soft material, KE1300T (Shin-Etsu Chemical) (Substituting C_{10} from Table 3 into the relationships $2C_{10} = G$ and $G = E/(2 + 2\nu)$ yields the elastic modulus E of KE1300T as $E = 1.3679$ MPa (average), which is relatively high compared to other elastomers.[55] Accordingly, the use of KE1300T with relatively high stiffness allows EGP II to mitigate distortion while maintaining a thin thickness t_1. Furthermore, this study achieves the user-desired

stretchability—which is generally difficult to attain with high-stiffness materials—through optimization of the pattern design). Here, $\{C_{10}, C_{20}, C_{30}\}$ are determined using an optimization method to ensure that the stretchability analysis results are consistent with the test results (the graph in the first row of Figure 4a).

While using the same element type, effective thicknesses, and material model as the stretchability analysis, the distortion analysis in Figure 4a models the finger body of the distortion test as a system of flat unit cells with a quarter-arc profile. In addition, the distortion analysis imposes thickness-directional displacement constraints on the left strap regions to include contact effects resulting from the finger-shaped rigid structure. The external forces applied by Tendon 1 are represented by $\{F_1, F_2\}$, which

ADVANCED
SCIENCE NEWS
www.advancedsciencenews.com

ADVANCED
INTELLIGENT
SYSTEMS
Open Access

www.advintellsyst.com

(a)

(b)

Figure 4. a) Numerical simulations equivalent to the tests in Figure 3a. The stretchability analysis employs RBE2, which rigidly connects dependent nodes to an independent node, to induce uniform extension at all top edge points (clamped condition). In the plots, the red spots and error bars represent the mean values and standard deviations of the experimental results, respectively, while the bar graphs correspond to the numerical simulation results. Together with the deformed shapes, the comparison between the simulation and experimental results demonstrates that the simulations can capture the actual nonlinear responses observed in the tests. b) Derivation of unit cell-level simulations from finger body-level simulations. This determines the internal nodal forces and moments that the unit cell is subjected to during the finger body-level simulations. In the unit cell-level simulations, the nodal forces/moments determined from the 1D analyses are applied to all the top edge points using RBE2, which also plays a role in inducing rigid-body translations and rotations at all the top edge points. The distance from the independent node of RBE2 to the top edge is zero (i.e., $e = 0$), although these points are separated in Figure 4b to ensure a clear visualization.

act on the right strap regions along the transverse and thickness directions, respectively. The magnitude of F_i ($i = 1$ or 2) exerted on each strap is assumed to be identical. The magnitudes of $\{F_1, F_2\}$ are determined using an optimization method to ensure that the distortion analysis results are consistent with the test results (the graph in the second row of Figure 4a).

Based on the distortion analysis, the value of $\hat{\beta}$ depicted in Figure 3c can be calculated. β can then be determined from $\hat{\beta}$ using the following relation (Figure 3c).

$$\hat{\beta} : \{r + \tfrac{t_1}{2}\} = \beta : \{r + t_1 + \tfrac{t_2 - t_1}{2}\} \tag{5}$$

## 4. Unit Cell-Level Simulations

This section describes the derivation of the unit cell-level simulations equivalent to the finger body-level simulations (Figure 4b). These unit cell-level simulations can evaluate the unit cell's distortional stiffness and stretchability, enabling the unit cell design optimization.

First, the finger body-level simulations are converted to equivalent 1D analyses, where each unit cell is represented by a straight line passing through its centerline (Figure 4b). In the 1D analyses, these straight lines are discretized using B31 (3D beam element with 1st-order interpolation), a typical 1D element in Abaqus. In addition, $\{F_1, F_2\}$, along with the reaction force F_R caused by the strap constraint, are replaced by the equivalent forces $\{F_1, F\}$ and moment M acting at the center of each straight line. Here, $\{F, M\}$ indicate the force and moment caused by $\{F_2, F_R\}$, and their magnitudes can be calculated using the following relations

$$F = F_R + F_2, \quad M = (F_R - F_2) \times \{(b_1 - b_3)/2\} \tag{6}$$

where $\{F_2, F_R, F\}$ have the same positive directions.

The 1D analyses yield the internal nodal forces, internal nodal moments, and strains for each unit cell (Figure 4b). To define stricter design requirements, we use the internal nodal forces and moments exerted on the unit cell that shows maximum strains and derive the corresponding unit cell-level analyses, as shown in **Figure 5**a. Specifically, the resulting nodal forces, nodal moments, and $\{F_1, F, M\}$ are classified such that the unit
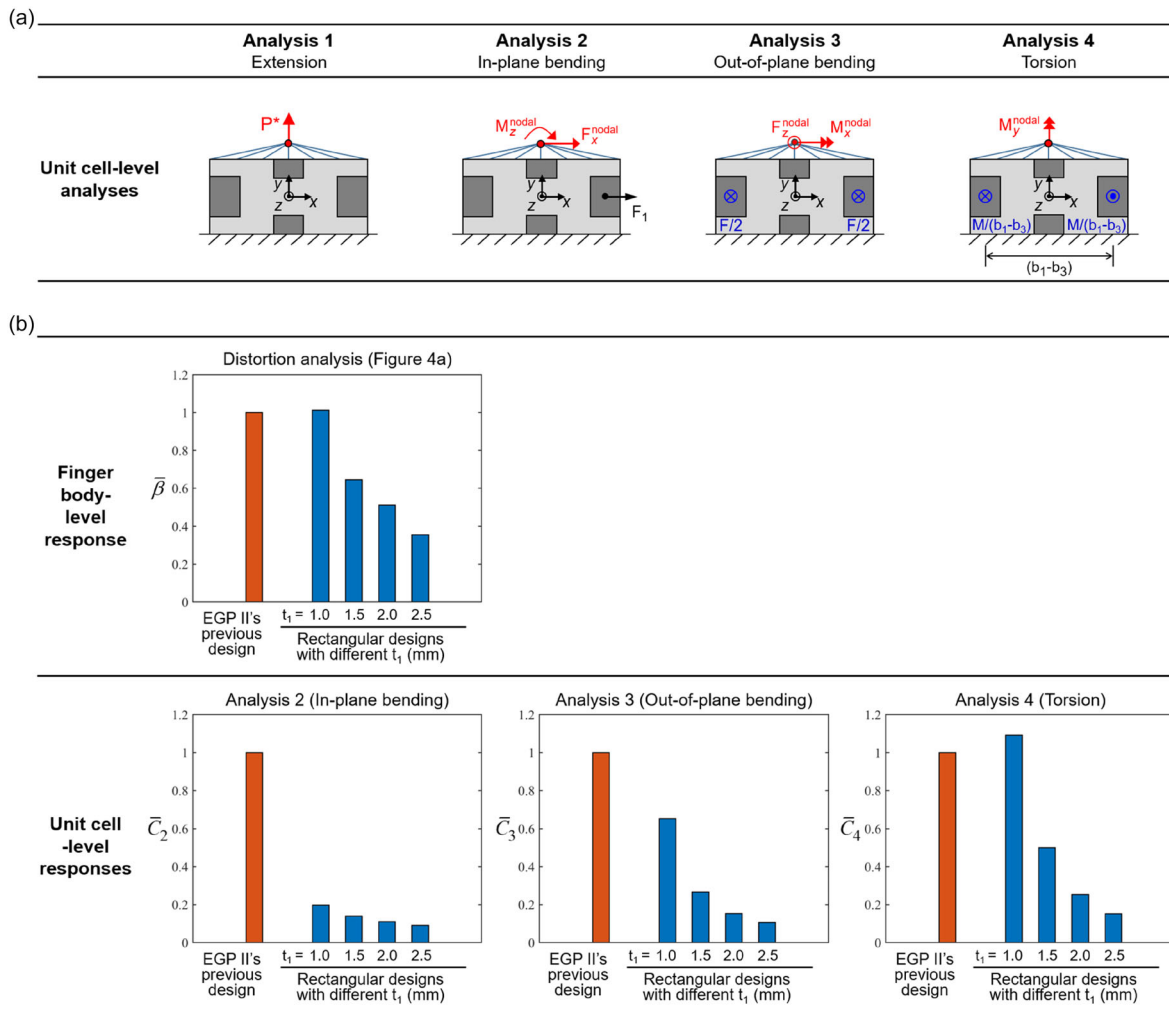
Figure 5. a) Unit cell-level analyses. Analysis 1 considers $P = P^*$ obtained from the sample-based preference test. b) Comparison of unit cell-level responses $\{\overline{C}_2, \overline{C}_3, \overline{C}_4\}$ in Equation (9) with the finger body-level response $\overline{\beta}$ in Equation (11).

cell-level analyses can measure four distinct types of stiffness, i.e., for extension, in-plane bending, out-of-plane bending, and torsion. In this regard, $\{F_1, F, M\}$ of the 1D analyses are replaced by the equivalent forces $\{F_1, F/2, M/(b_1 - b_3)\}$ acting on the strap regions.

5. Optimization Problem Formulation

This section formulates an optimization problem for a unit cell that minimizes the distortional compliance while satisfying the stretchability constraint. To this end, we define distortional compliance as the weighted sum of the compliances corresponding to the unit cell-level analyses, as detailed below.

Using the unit cell-level analyses (Figure 5a), the optimization problem can be formulated as

$$
\begin{aligned}
\text{Minimize} \quad & w_2 \overline{C}_2 + w_3 \overline{C}_3 + w_4 \overline{C}_4 \\
\text{Subject to:} \quad & C_1 - C_1^* = 0 \\
& x\text{-}\,\text{and}\;y\text{-}\,\text{axis}\;\text{symmetry}
\end{aligned}
\tag{7}
$$

where C_k ($k = 1,2,3,4$) represents the compliance (inverse of stiffness) of the unit cell corresponding to Analysis k and can be calculated using the following equation.

$$
C_k = \mathbf{d}_k^T \mathbf{F}_k
\tag{8}
$$

In Equation (8), $\mathbf{d}_k$ and $\mathbf{F}_k$ denote the nodal displacement vector and external nodal force vector, respectively, defined for all nodes in Analysis k. $\overline{C}_k$ ($k = 1, 2, 3, 4$) in Equation (7) represents a normalized compliance, which is defined as

$$
\overline{C}_k = C_k / C_k^{\text{pre}}
\tag{9}
$$

where C_k^{pre} represents C_k for the unit cell having the EGP II's previous design (Figure 1a).

Accordingly, Equation (7) represents the compliance minimization problem under multiple loading conditions.[50] Here, the objective function is defined as the weighted sum of the normalized compliances corresponding to Analyses 2–4 derived from the distortion analysis. Minimizing this objective function yields the unit cell design with the minimum β. To satisfy the user-selected stretchability, Equation (7) also includes $C_1 = C_1^*$ as an equality constraint, where C_1^* denotes the C_1 value corresponding to the sample selected in the preference test (Figure 3b). Finally, Equation (7) considers both x-axis and y-axis symmetry conditions, which ensure that the optimal solution can be applied to all unit cell locations on the index and middle finger bodies.

In Equation (7), the weighting factor w_k ($k = 2, 3, 4$) represents the priority of reducing C_k to prevent β and is calculated based on the relation between $\overline{\beta}$ and $\overline{C}_k$

$$
w_k = \frac{\sum_{j=1}^{4} \left\{ 1 - |\overline{C}_k(t_1 = \frac{j+1}{2}) - \overline{\beta}(t_1 = \frac{j+1}{2})| \right\}}{4}
\tag{10}
$$

where $\overline{\beta}$ denotes a normalized distortion, which is defined as

$$
\overline{\beta}(t_1) = \beta(t_1) / \beta^{\text{pre}}
\tag{11}
$$

In Equation (11), β^{pre} indicates the β value for the finger body with the EGP II's previous design.

To clarify the meaning of Equation (10), we consider $\overline{C}_2(t_1 = 1)$ and $\overline{\beta}(t_1 = 1)$ as representative examples. As shown in Figure 5b, $\overline{C}_2(t_1 = 1) = 0.2$ indicates that the in-plane bending stiffness of the rectangular pattern with $t_1 = 1$ nm is five times greater than that of EGP II's previous design. In contrast, $\overline{\beta}(t_1 = 1) = 1.0$ states that the distortional stiffness of the finger body with the rectangular pattern with $t_1 = 1$ nm is the same as that of the EGP II's previous design. Based on these observations, the priority of C_2 can be quantified as $\{1 - |\overline{C}_2(t_1 = 1) - \overline{\beta}(t_1 = 1)|\}$, which is close to 1 if C_2 has a high priority in enhancing distortional stiffness. Accordingly, $\{1 - |\overline{C}_2(t_1 = 1) - \overline{\beta}(t_1 = 1)|\} = 0.2$ indicates that C_2 has a low priority (i.e., minimizing C_2 is less effective in preventing β). Since $\{1 - |\overline{C}_2(t_1) - \overline{\beta}(t_1)|\}$ can be calculated for unit cells with the rectangular pattern with $t_1 = 1.0, 1.5, 2.0$, and 2.5 mm, we define their average as w_2. Moreover, $\{w_3, w_4\}$ are calculated in the same manner as expressed in Equation (10). (The weighting factor w_k ($k = 2, 3, 4$) varies depending on the modeling of the finger body-level simulations. For instance, if the contact effect (i.e., the displacement constraints on the left straps) described in Section 4 is not considered, this absence leads to sequential variations in the distortion analysis results, the derived loading conditions for the unit cell-level analyses, the compliance values C_k, and the corresponding weighting factors w_k, ultimately resulting in a different optimized design. This study establishes finger body-level simulations whose results closely match the experimental data, thereby enabling an optimized unit cell design that satisfies all the design requirements.)
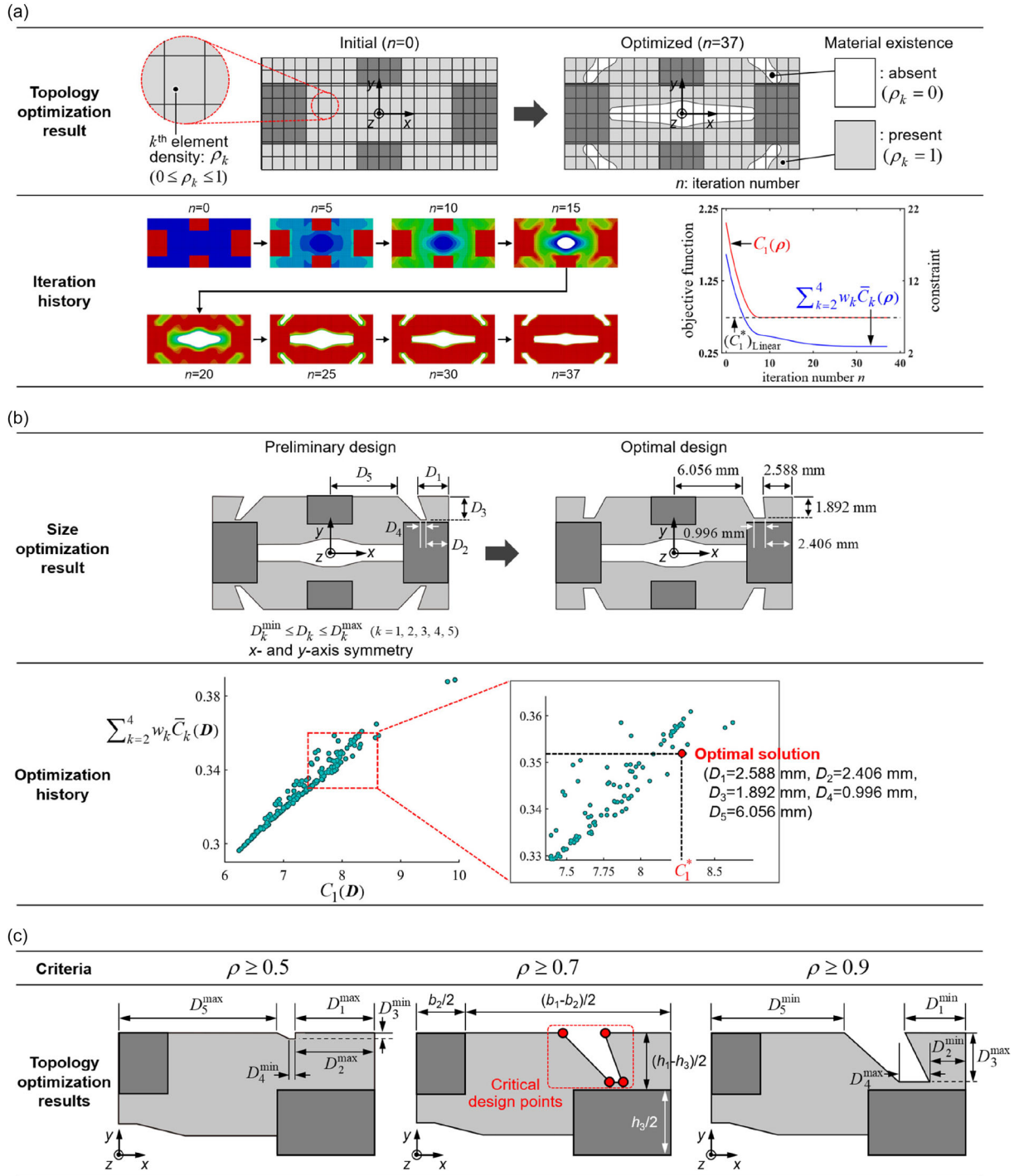
6. Two-Step Optimization Approach

To determine the optimal material layout for Equation (7) within the design domain defined in Figure 2, topology optimization is first performed. At this stage, a linear elastic assumption is employed to ensure convergence of the solution. Subsequently, using the topology optimization result as a preliminary design, size optimization is carried out to incorporate material and geometric nonlinearities. This two-step approach enables the derivation of an optimal solution that satisfies the design requirements under large deformations. Further details on this two-step approach are provided below.

6.1. Topology Optimization Based on Linear Elastic Assumption

The topology optimization formulation for Equation (7) can be expressed as

$$
\begin{aligned}
\underset{\boldsymbol{\rho} \in R^N}{\text{Minimize}} \quad & w_2 \overline{C}_2(\boldsymbol{\rho}) + w_3 \overline{C}_3(\boldsymbol{\rho}) + w_4 \overline{C}_4(\boldsymbol{\rho}) \\
\text{Subject to:} \quad & (C_1^*)_{\text{Linear}} - C_1(\boldsymbol{\rho}) \leq 0 \\
& 0 \leq \rho_k \leq 1 \quad (k = 1, 2, \ldots, N) \\
& x\text{-}\,\text{and}\;y\text{-}\,\text{axis}\;\text{symmetry}
\end{aligned}
\tag{12}
$$

where the design variables are $\boldsymbol{\rho} = \{\rho_1, \ldots, \rho_N\}$ (N: number of elements), and ρ_k represents the material density of the kth shell element in the design domain (**Figure 6**a). Accordingly, unit cells with different $\boldsymbol{\rho}$ values have different values of $\{\overline{C}_1, \overline{C}_2, \overline{C}_3, \overline{C}_4\}$.

**ADVANCED
SCIENCE NEWS**

www.advancedsciencenews.com

**ADVANCED
INTELLIGENT
SYSTEMS**
Open Access

www.advintellsyst.com

Figure 6. a) Topology optimization results for Problem 1. The topology optimization considers $\boldsymbol{\rho} = \{\rho_1, \rho_2, \dots, \rho_N\}$ (N: number of shell elements) as the design variables. Here, ρ_k represents the material density of the kth shell element. b) Size optimization results for Problem 1. The result in Figure 6a is simplified first using straight lines and is then used as the preliminary design. The size optimization uses $\boldsymbol{D} = \{D_1, D_2, D_3, D_4, D_5\}$ as the design variables. c) Comparison of topology optimization results with different plot criteria. Owing to the x-axis and y-axis symmetry, only the segment in Quadrant I ($x \geq 0$, $y \geq 0$) is considered. From this comparison, we determine the design variable D_k ($k = 1, 2, 3, 4, 5$) and its bounds $\{D_k^{\min}, D_k^{\max}\}$.

The continuous variable ρ_k ($k = 1, 2, \dots, N$) can have any value in the range $0 \leq \rho_k \leq 1$ and its initial value is set to 0.5. Through topology optimization, ρ_k converges to 0 or 1, which indicates the absence or presence of the material in the kth element, respectively. To obtain a converged solution for ρ_k, we employ the solid isotropic material with penalization method[56]
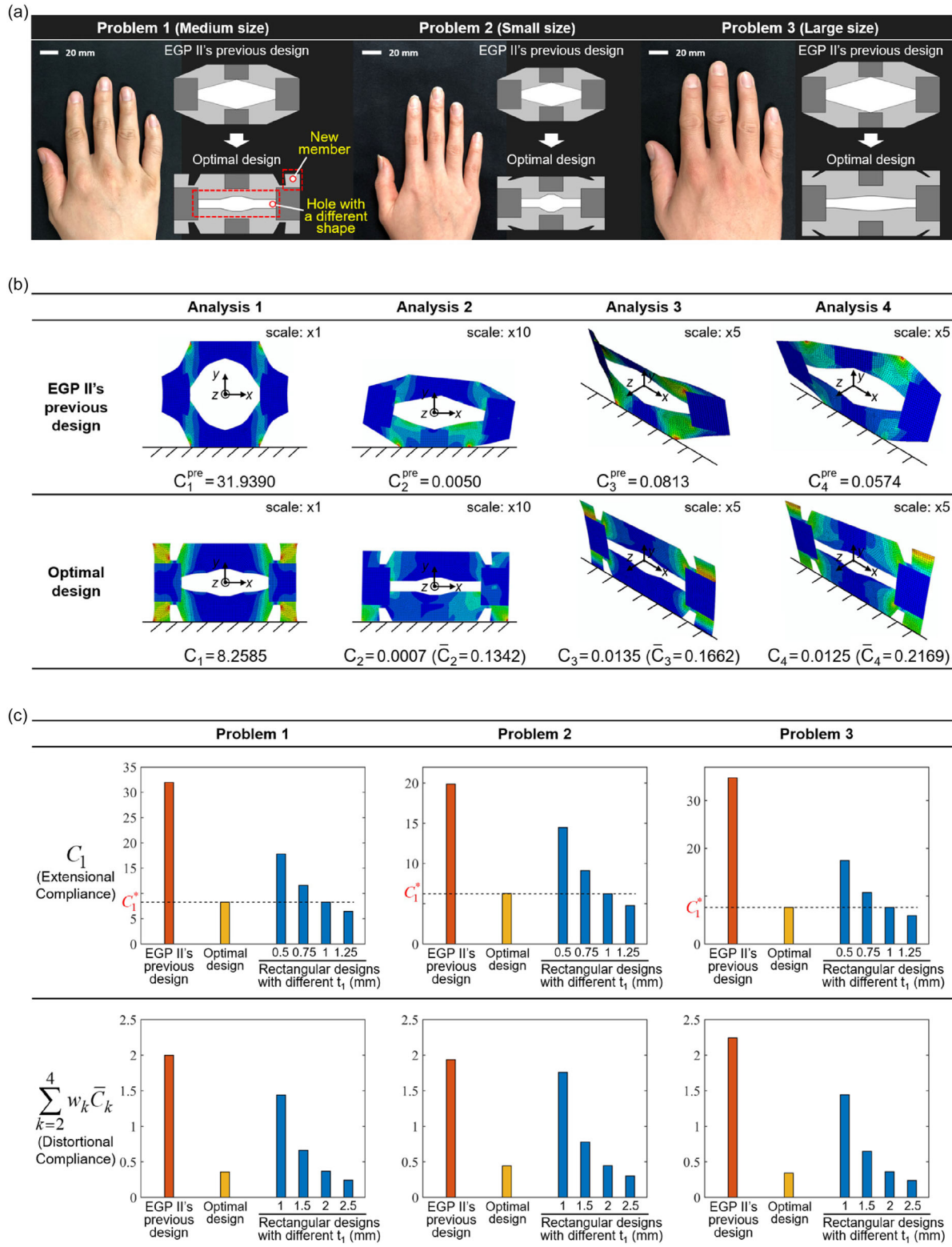
Figure 7. a) Problems 1–3 considering three users with different hand sizes (Table 1) and the corresponding optimal unit cell designs. For comparison, EGP II's previous designs, which are sized to fit the user's hands, are also shown. b) Responses of optimal unit cell design for Problem 1 in unit cell-level analyses. Deformed shapes, color-mapped von Mises stresses, and compliances are included. c) C_1 and $\sum_{k=2}^{4} w_k \overline{C}_k$ for optimal designs (Table 7). Data of EGP II's previous designs and rectangular designs are included for comparison.

with a penalization parameter $p = 3$. For the same purpose, we use the method of moving asymptotes (MMA)[57] as the optimization algorithm.

Instead of C_1^*, Equation (12) considers $(C_1^*)_{\text{Linear}}$, which is obtained via a linear analysis, to maintain consistency with the linear elastic assumption. While $C_1(\boldsymbol{\rho}) \geq (C_1^*)_{\text{Linear}}$ is used, the inequality constraint plays the same role as $C_1(\boldsymbol{\rho}) = (C_1^*)_{\text{Linear}}$ (i.e., active) during optimization, so that the MMA algorithm can find the optimal unit cell design that minimizes the objective function $w_2 \overline{C}_2(\boldsymbol{\rho}) + w_3 \overline{C}_3(\boldsymbol{\rho}) + w_4 \overline{C}_4(\boldsymbol{\rho})$ within the imposed constraint.

6.2. Size Optimization Considering Material and Geometric Nonlinearities

The topology optimization result that includes only those elements for which ρ converges to 1 can be used as a preliminary design for the subsequent size optimization[58] (Figure 6b). Moreover, a comparison between topology optimization results with different plot criteria, from $\rho \geq 0.5$ to $\rho \geq 0.9$ (Figure 6c), suggests the design variables suitable for size optimization.

Specifically, Figure 6c shows that elements with intermediate density values are located around the critical design points. This indicates that the design change around the critical design points plays a crucial role in achieving both the stretchability that meets $C_1 \geq (C_1^*)_{\text{Linear}}$ and the distortional stiffness that minimizes $w_2 \overline{C}_2 + w_3 \overline{C}_3 + w_4 \overline{C}_4$. Accordingly, the $\{D_1, D_2, D_3, D_4, D_5\}$ values (Figure 6b) that determine the locations of these design points are defined as the design variables, and their corresponding bounds $\{D_k^{\min}, D_k^{\max}\}$ ($k = 1, 2, 3, 4, 5$) are determined based on the results in Figure 6c.

Based on $\boldsymbol{D} = \{D_1, D_2, D_3, D_4, D_5\}$, the size optimization formulation for Equation (7) can be expressed as

$$\underset{\boldsymbol{D} \in R^5}{\text{Minimize}} \quad w_2 \overline{C}_2(\boldsymbol{D}) + w_3 \overline{C}_3(\boldsymbol{D}) + w_4 \overline{C}_4(\boldsymbol{D})$$

$$\text{Subject to}: \quad C_1(\boldsymbol{D}) - C_1^* = 0$$
$$\boldsymbol{D} = \{D_1, D_2, D_3, D_4, D_5\} \qquad (13)$$
$$D_k^{\min} \leq D_k \leq D_k^{\max} \quad (k = 1, 2, 3, 4, 5)$$
$$x - \text{ and } y - \text{axis symmetry}$$

where the constraint considers C_1^*, which is obtained via the nonlinear analysis. To find the global optimal solution of $\boldsymbol{D}$ for Equation (13), we employ the nondominated sorting genetic algorithm II (NSGA II).[59]

7. Finger Body Optimization

We solve three optimization problems that consider three users with different hand sizes (**Figure 7**a). Using the proposed design method, we define the corresponding design domains, finger body-level tests and analyses, unit cell-level analyses, and optimization formulations. The results are summarized in **Table 1, 2, 3, 4**, and **5**.

Subsequently, we conduct topology optimization for Problems 1, 2, and 3. As an example, the optimization history and result of Problem 1 are given in Figure 6a, where the design domain

Table 1. Dimensions (mm) of finger body and its periodic unit cell (Figure 2).

	L_1	L_2	b_1	b_2	b_3	h_1	h_2	h_3	t_1	t_2	t_3
Problem 1	73	83	21	4	4	10	2.5	5.38	2.5	5.8	20
Problem 2	67	76	18	4	4	9	2.5	4.84	2.5	5.8	17
Problem 3	79	90	23	4	4	11	2.5	5.92	2.5	5.8	22

Table 2. Parameters for finger body-level tests (Figure 3).

	α [mm]	P^* [N]	r [mm]	d [mm]	T^* [N]
Problem 1	13	5.896	6.50	1.65	0.634
Problem 2	12	4.952	5.00	1.65	0.562
Problem 3	13	5.572	7.50	1.65	0.830

is discretized into 3,360 shell elements with a size of 0.25×0.25 mm (i.e., $N = 3,360$). The element size is set to be small enough to serve fully converged analysis results. The iteration history in Figure 6a shows that $\boldsymbol{\rho}$ in Equation (12) converges after 45 iterations (27 min), and the resulting $\boldsymbol{\rho}$ minimizes $\sum_{k=2}^{4} w_k \overline{C}_k(\boldsymbol{\rho})$ while satisfying the constraint $C_1(\boldsymbol{\rho}) = (C_1^*)_{\text{Linear}}$. Once Equation (12) is solved, our two-step approach can determine the corresponding bounds of $\boldsymbol{D}$ in Equation (13) (Figure 6c). The results are presented in **Table 6**.

Finally, we conduct size optimization for Problems 1, 2, and 3. Figure 6b presents the optimization history and result of Problem 1 as an example. To find the optimal solution of $\boldsymbol{D}$ in Equation (13), 240 candidates (population size: 12, and number of generations: 20) are considered in NSGA-II. The optimization takes 162 min when using shell elements with a size of 0.25×0.25 mm. The optimization history in Figure 6b plots $C_1(\boldsymbol{D})$ and $\sum_{k=2}^{4} w_k \overline{C}_k(\boldsymbol{D})$ for the 240 candidates, showing that the optimal solution $\boldsymbol{D}^{\text{optimal}}$ satisfies $C_1(\boldsymbol{D}) = C_1^*$ and minimizes $\sum_{k=2}^{4} w_k \overline{C}_k(\boldsymbol{D})$. **Table 7** lists the size optimization results.

Figure 7a shows the optimal unit cell designs. Compared with the EGP II's previous design, the optimal designs have a differently shaped hole and include new members connecting the strap regions of adjacent unit cells (**Figure 8**a).

The optimal designs are examined via unit cell-level analyses. Figure 7b presents the results for Problem 1 as an example, where the color-mapped stress distributions highlight that the new members play a crucial role in reducing the distortion-related compliances $\{C_2, C_3, C_4\}$. Additionally, the deformed configurations show that the resulting hole shape enables the optimal design to achieve the desired tensile compliance C_1.

These new features allow the optimal designs to satisfy all the requirements in Equation (7), while the EGP II's previous design and the rectangular designs with different thicknesses cannot (Figure 7c). Specifically, the $\sum_{k=2}^{4} w_k \overline{C}_k$ values of the optimal designs for Problems 1, 2, and 3 are approximately 17.7%, 22.7%, and 15.4%, respectively, of the corresponding values for the EGP II's previous designs. The optimal designs for Problems 1, 2, and 3 have C_1 values similar to the rectangular

Table 3. Parameters for finger body-level simulations (Figure 4a).

	t_2^e [mm]	t_3^e [mm]	C_{10}	C_{20}	C_{30}	F_1 [N]	F_2 [N]
Problem 1	5.37	13.79	0.2362	−0.0272	0.0244	0.0230	0.0471
Problem 2	5.37	11.81	0.2274	−0.0482	0.0252	0.0186	0.0416
Problem 3	5.37	14.93	0.2320	−0.0272	0.0193	0.0252	0.0332

Table 4. External loads (N, mm) used in unit cell-level analyses (Figure 5a).

	P^*	F_1	$F/2$	$M/(b_1-b_3)$	F_x^{nodal}	F_z^{nodal}	M_x^{nodal}	M_y^{nodal}	M_z^{nodal}
Problem 1	5.896	0.0230	0.0755	0.0314	0.009	0.059	0.140	0.753	0.191
Problem 2	4.952	0.0186	0.0617	0.0259	0.006	0.046	0.124	0.538	0.167
Problem 3	5.572	0.0252	0.0526	0.0251	0.016	0.037	0.101	0.606	0.215

Table 5. Constraint values and weighting factors for optimization problems (Equation (12) and (13)).

	C_1^*	$(C_1^*)_{Linear}$	w_2	w_3	w_4
Problem 1	8.247	6.890	0.504	0.664	0.829
Problem 2	6.230	5.024	0.483	0.709	0.743
Problem 3	7.614	6.434	0.635	0.762	0.847

Table 6. Bounds (mm) for design variables $\boldsymbol{D} = \{D_1, D_2, D_3, D_4, D_5\}$ in equation (13).

	D_1^{min}	D_1^{max}	D_2^{min}	D_2^{max}	D_3^{min}	D_3^{max}	D_4^{min}	D_4^{max}	D_5^{min}	D_5^{max}
Problem 1	2.50	3.25	1.50	3.25	0.25	2.05	0.25	1.25	5.50	6.50
Problem 2	2.25	3.00	1.50	3.00	0.50	1.83	0.25	1.25	3.75	5.00
Problem 3	2.75	3.25	1.50	3.50	0.25	2.25	0.25	1.25	7.00	8.00

design with $t_1 = 1$ mm while having $\sum_{k=2}^{4} w_k \overline{C}_k$ values similar to the rectangular design with $t_1 = 2$ mm (Figure 7c).

Substituting the optimal unit cell designs for Problems 1, 2, and 3 into the design domain (Figure 2) yields the corresponding optimal finger bodies. The resulting optimal index finger bodies are shown in Figure 8a.

The optimal finger bodies are examined via the aforementioned tests (Figure 3a) and simulations (Figure 4a), and the results are shown in Figure 8b,c. The new features of the optimal unit cells allow the optimal finger bodies to exhibit the desired responses in the tests (Figure 8b); thus these finger bodies satisfy all the design requirements defined in Section 3.1 (Figure 8c),

while the EGP II's previous design and the rectangular designs with different thicknesses cannot. Specifically, the stretchability test results show that the optimal finger bodies for Problems 1, 2, and 3 elongate by α (Table 2) under $P = 5.30$ N (error: 8.5%), 5.18 N (error: 3.7%), and 5.71 N (error: 1.1%), respectively. The distortion test results show that the β values of the optimal finger bodies for Problems 1, 2, and 3 are ≈46.7%, 51.2%, and 37.5% of those of the EGP II's previous designs, respectively. Notably, the optimal designs for Problems 1, 2, and 3 have stretchability levels similar to that of the rectangular design with $t_1 = 1$ mm while exhibiting β values similar to that of the rectangular design with $t_1 = 2$ mm; this is consistent with the results for the optimal unit cells (Figure 7c).

Using the obtained finger body design for Problems 1, 2, and 3, we fabricate an optimized EGP II for the corresponding users. **Figure 9**a depicts the optimized EGP II for Problem 1 as an example. The flexion motions of the optimized EGP II are tested using the experimental setup shown in Figure 9b. A slider-tendon linear actuator (STLA)[60] is used to control the tensile force T applied to Tendon 1 (Figure 1a). The responses of the electromyography (EMG) sensors (Delsys) are observed to ensure that the user's muscles are inactive during the test.[61] The results show that the optimized EGP II is almost undistorted during flexion (Figure 9c) while providing the desired wearability.

The changes in grasping force of the optimized EGP II, compared to the previous version, are experimentally investigated (Figure 9d). For a fair comparison, the length of the spring sheath (Bowden cable), which helps transmit the tensile force T from the STLA to EGP II, is kept identical. The tensile force T of the actuation wire within the sheath is precisely controlled to reach its target value using the STLA. Under the given tensile

Table 7. Optimal solution $\boldsymbol{D}^{\mathrm{optimal}}$ and corresponding performance metrics.

	D_1^{optimal} [mm]	D_2^{optimal} [mm]	D_3^{optimal} [mm]	D_4^{optimal} [mm]	D_5^{optimal} [mm]	$C_1(\boldsymbol{D}^{\mathrm{optimal}})$	$\sum_{k=2}^{4} w_k \overline{C}_k(\boldsymbol{D}^{\mathrm{optimal}})$
Problem 1	2.588	2.406	1.892	0.996	6.056	8.246	0.358
Problem 2	2.675	1.773	0.664	0.404	4.426	6.267	0.442
Problem 3	3.105	1.683	1.073	0.352	7.534	7.616	0.342
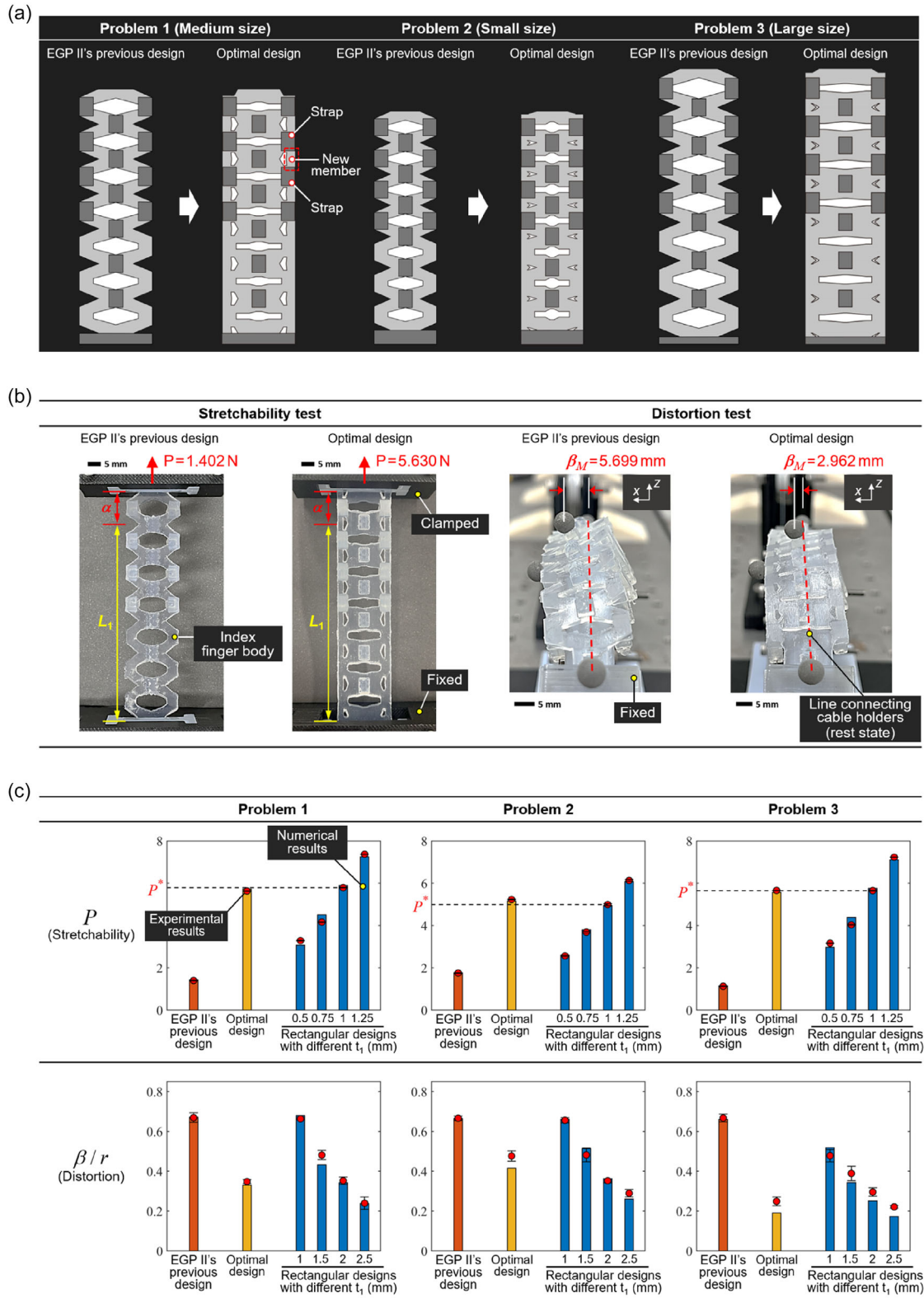
Figure 8. a) Optimal finger body designs. Index finger bodies comprising seven unit cells are shown as an example. b) Responses of optimal finger body for Problem 1 in finger body-level tests. c) Finger body-level test and simulation results (Figure 3a and 4a). In these plots, the red spots and error bars represent the mean values and standard deviations of the experimental results, respectively, while the bar graphs correspond to the numerical simulation results. In addition, P denotes the force that elongates the finger body by α, while β/r represents the ratio of the distortion β to the radius r of the finger-shaped rigid structure (Figure 3a).
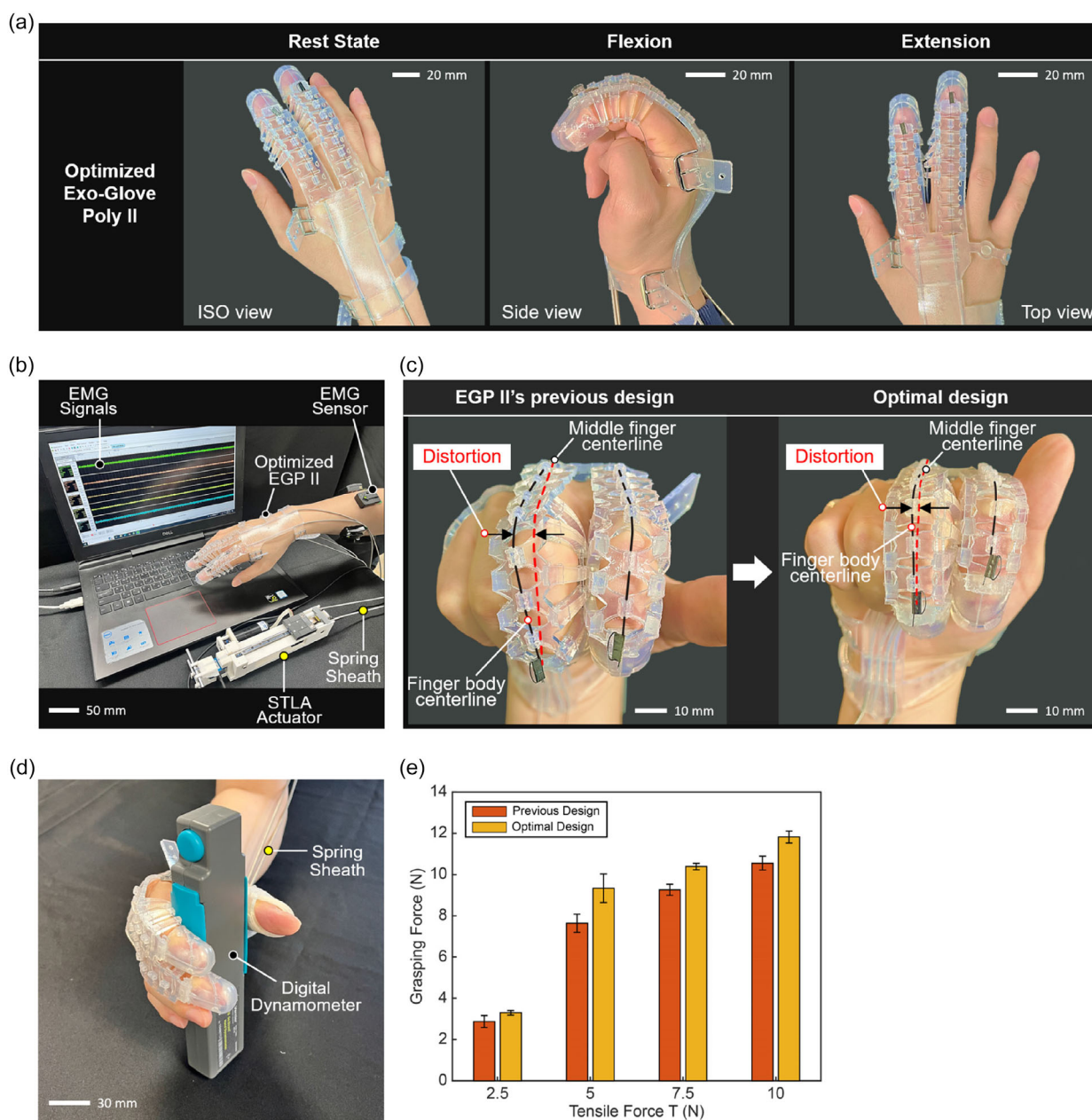
Figure 9. a) Optimized EGP II. b) Test setup for evaluating EGP II's flexion motion. The STLA is used to control the actuation speed and the magnitude of the applied tensile force *T*. Five EMG sensors are used to ensure that the user's muscles remain inactive during the test. c) Flexion motions observed in the test. Unlike the previous EGP II, the optimized EGP II exhibits almost no distortion during flexion while providing the desired wearability. d) Test setup used to evaluate the grasping force of EGP II. e) Grasping force measurement results. For each tensile force *T*, the dynamometer is grasped five times. In the plot, the bar graphs and error bars represent the mean grasping forces and standard deviations, respectively.

force T, the corresponding grasping force is measured using a digital dynamometer (Go Direct Hand Dynamometer, Vernier). Specifically, the dynamometer is positioned within the hand aperture—between the thumb and the index/middle fingers—and the grasping force is measured using a medium-wrap grasp configuration.

The measurement results are presented in Figure 9e, indicating that the grasping force of the optimized EGP II is increased by 15.3% on average compared to the previous version. This observation suggests that the optimized finger body design successfully minimizes constraints on the user's flexion motion by fulfilling the user-preferred stretchability, thereby achieving the target finger posture without a significant increase in tensile force T. Furthermore, it implies that the increase in grasping force is achieved by improving force transmission, which was potentially degraded in the previous version due to distortion.

8. Conclusions

This study newly proposed a finger body design method for EGP II. By considering the finger body as a patterned structure with longitudinal periodicity, we simplified the design domain as a single-periodic unit cell (Figure 2). To evaluate the unit cell's distortional stiffness and stretchability, we established finger body-level tests and simulations (Figure 3a and 4a) and then derived equivalent unit cell-level analyses (Figure 4b). To formulate the optimization problem, we defined the unit cell's distortional compliance as a weighted sum of the compliances corresponding to the unit cell-level analyses and used it as the objective function (Equation (7–11) and Figure 6b). To satisfy the design requirements under large deformations, an optimal solution was obtained through a two-step optimization approach. Specifically, the optimal material layout within the given design domain was determined using topology optimization under a linear elastic assumption (Figure 6a). Using the topology optimization result as a preliminary design, size optimization was then conducted to incorporate material and geometric nonlinearities, leading to the final optimized solution (Figure 6b).

To validate the proposed method, we solved three optimization problems considering three users with different hand sizes (Table 1, 2, 3, 4, 4, 5, 6, and 7). The performance of the obtained unit cell designs (Figure 7a) was measured through the established unit cell-level and finger body-level evaluations. The results showed that our optimal designs achieved the distortional stiffness levels similar to that of the rectangular design with $t_1 = 2$ mm while also providing stretchability levels similar to that of the rectangular design with $t_1 = 1$ mm (Figure 7c and 8c). Specifically, the finger body-level tests showed that the optimal designs exhibited, on average, 54.9% less distortion than the EGP II's previous designs under the same tensile force T while providing the target stretchability with an average error of 4.43%. Consequently, EGP II with the optimal finger body design showed almost no distortion while providing the desired wearability (Figure 9c). Moreover, the optimized EGP II achieves a 15.3% average increase in grasping force compared to the previous version (Figure 9e). These results confirm that our method can find an optimal finger body design that not only helps EGP II attain its target functionality by preventing distortion but also provides the desired wearability for users with different hand sizes. Moreover, two key design aspects—1) a tailored fit achieved by customizing the finger-body dimensions based on the user's finger measurements and 2) minimized motion constraints achieved by fulfilling the user-preferred stretchability—enhance the conformability of EGP II, thereby improving comfortability for the users. We expect that the proposed method can be extended to soft body designs not only for other tendon-driven soft wearable robots that require both distortion prevention and stretchability, but also for tendon-driven continuum robots[62,63] that demand high torsional stiffness and dexterity.

Acknowledgements

Conflict of Interest

The authors declare no conflict of interest.

Data Availability Statement

The data that support the findings of this study are available from the corresponding author upon reasonable request.

Keywords

[1] M. Xiloyannis, R. Alicea, A.-M. Georgarakis, F. L. Haufe, P. Wolf, L. Masia, R. Riener, *IEEE Trans. Robot.* **2021**, *38*, 1343.

[2] M. Pan, C. Yuan, X. Liang, T. Dong, T. Liu, J. Zhang, J. Zou, H. Yang, C. Bowen, *Adv. Intell. Syst.* **2022**, *4*, 2100140.

[3] T. Bützer, O. Lambercy, J. Arata, R. Gassert, *Soft Robot.* **2021**, *8*, 128.

[4] B. Sharma, P. T. Phan, J. Davies, T. T. Hoang, C. C. Nguyen, A. Ji, K. Zhu, E. Nicotra, N. H. Lovell, T. N. Do, *Adv. Intell. Syst.* **2024**, *6*, 2400266.

[5] D. Lee, S. Lee, D. Lee, D. Shin, *Adv. Intell. Syst.* **2025**, *7*, 2400700.

[6] H. In, B. B. Kang, M. Sin, K.-J. Cho, *IEEE Robot. Autom. Mag.* **2015**, *22*, 97.

[7] B. Kim, H. In, D.-Y. Lee, K.-J. Cho, *J. NeuroEng. Rehabil.* **2017**, *14*, 1.

[8] D. Chiaradia, L. Tiseni, M. Xiloyannis, M. Solazzi, L. Masia, A. Frisoli, *Front. Robot. AI* **2021**, *7*, 595862.

[9] N. Lotti, M. Xiloyannis, G. Durandau, E. Galofaro, V. Sanguineti, L. Masia, M. Sartori, *IEEE Robot. Autom. Mag.* **2020**, *27*, 43.

[10] R. J. Varghese, B. P. L. Lo, G.-Z. Yang, *IEEE Robot. Autom. Lett.* **2020**, *5*, 540.

[11] D. Pyeon, J. Ahn, D. H. Kim, S. Cheon, G. Jeong, K.-J. Cho, *IEEE Robot. Autom. Lett.* **2024**, *9*, 9613.

[12] D. Park, K.-J. Cho, *PLoS One* **2017**, *12*, e0173730.

[13] S.-S. Yun, K. Kim, J. Ahn, K.-J. Cho, *Sci. Robot.* **2021**, *6*, eabe1243.

[14] H. D. Yang, M. Cooper, A. Eckert-Erdheim, D. Orzel, C. J. Walsh, *IEEE Robot. Autom. Lett.* **2022**, *7*, 7439.

[15] A. T. Asbeck, R. J. Dyer, A. F. Larusson, C. J. Walsh, *IEEE Int. Conf. Rehabil. Robot.* **2013**, 1.

[16] A. T. Asbeck, S. M. De Rossi, K. G. Holt, C. J. Walsh, *Int. J. Robot. Res.* **2015**, *34*, 744.

[17] G. Lee, J. Kim, F. Panizzolo, Y. M. Zhou, L. M. Baker, I. Galiana, P. Malcolm, C. J. Walsh, *Sci. Robot.* **2017**, *2*, eaan6708.

[18] Y. Ding, M. Kim, S. Kuindersma, C. J. Walsh, *Sci. Robot.* **2018**, *3*, eaar5438.

[19] C. Siviy, J. Bae, L. Baker, F. Porciuncula, T. Baker, T. D. Ellis, L. N. Awad, C. J. Walsh, *IEEE Robot. Autom. Lett.* **2020**, *5*, 828.

**ADVANCED
SCIENCE NEWS**

www.advancedsciencenews.com

**ADVANCED
INTELLIGENT
SYSTEMS**

www.advintellsyst.com

[20] R. W. Nuckols, S. Lee, K. Swaminathan, D. Orzel, R. D. Howe, C. J. Walsh, *Sci. Robot.* **2021**, *6*, eabj1362.

[21] J. Kwon, J.-H. Park, S. Ku, Y. Jeong, N.-J. Paik, Y.-L. Park, *IEEE Robot. Autom. Lett.* **2019**, *4*, 2547.

[22] C. Kim, G. Kim, Y. Lee, G. Lee, S. Han, D. Kang, S. H. Koo, J. Koh, *Smart Mater. Struct.* **2020**, *29*, 055003.

[23] S. Lee, N. Karavas, B. T. Quinlivan, D. L. Ryan, D. Perry, A. Eckert-Erdheim, P. Murphy, T. G. Goldy, N. Menard, M. Athanassiu, J. Kim, G. Lee, I. Galiana, C. J. Walsh, *IEEE Int. Conf. Robot. Autom.* **2018**, 2812.

[24] I. Galiana, F. L. Hammond, R. D. Howe, M. B. Popovic, *IEEE/RSJ Int. Conf. Intell. Robots Syst.* **2012**, 317.

[25] B. K. Dinh, M. Xiloyannis, L. Cappello, C. W. Antuvan, S.-C. Yen, L. Masia, *Robot. Auton. Syst.* **2017**, *92*, 173.

[26] H. In, U. Jeong, H. Lee, K.-J. Cho, *IEEE-ASME Trans. Mechatron.* **2016**, *22*, 159.

[27] J. Hughes, A. Spielberg, M. Chounlakone, G. Chang, W. Matusik, D. Rus, *Adv. Intell. Syst.* **2020**, *2*, 2000002.

[28] S. Wang, C. Zhao, S. Liu, Y. Li, Z. Xie, L. Chen, X. Yu, F. Yuan, Q. Zhang, M. Liu, L. Wen, *Adv. Intell. Syst.* **2024**, *6*, 2300127.

[29] T. Kermavnar, V. Power, A. de Eyto, L. W. O'Sullivan, *Soft Robot.* **2018**, *5*, 1.

[30] T. Kermavnar, V. Power, A. de Eyto, L. O'Sullivan, *Soft Robot.* **2018**, *5*, 497.

[31] M. B. Yandell, D. M. Ziemnicki, K. A. McDonald, K. E. Zelik, *PLoS One* **2020**, *15*, e0228536.

[32] H. Choi, B. B. Kang, B.-K. Jung, K.-J. Cho, *IEEE Robot. Autom. Lett.* **2019**, *4*, 4499.

[33] B. B. Kang, H. Choi, H. Lee, K.-J. Cho, *Soft Robot.* **2019**, *6*, 214.

[34] B. B. Kang, D. Kim, H. Choi, U. Jeong, K. B. Kim, S. Jo, K.-J. Cho, *IEEE Robot. Autom. Lett.* **2020**, *5*, 946.

[35] D. Kim, B. B. Kang, K. B. Kim, H. Choi, J. Ha, K.-J. Cho, S. Jo, *Sci. Robot.* **2019**, *4*, eaav2949.

[36] U. Jeong, K. Kim, S.-H. Kim, H. Choi, B. D. Youn, K.-J. Cho, *Int. J. Robot. Res.* **2021**, *40*, 494.

[37] J. Bae, K. Kong, M. Tomizuka, *ASME Dyn. Syst. Control Conf.* **2010**, 777.

[38] M. Zhang, V. Roberts, *J. Biomed. Eng.* **1993**, *15*, 451.

[39] K. Bertoldi, V. Vitelli, J. Christensen, M. Van Hecke, *Nat. Rev. Mater.* **2017**, *2*, 1.

[40] G. W. Milton, A. V. Cherkaev, *J. Eng. Mater. Technol.-Trans. ASME* **1995**, *117*, 483.

[41] M. Kadic, T. Bückmann, N. Stenger, M. Thiel, M. Wegener, *Appl. Phys. Lett.* **2012**, *100*, 19.

[42] A. Alomarah, S. H. Masood, D. Ruan, *Smart Mater. Struct.* **2022**, *31*, 025026.

[43] M. Schenk, S. D. Guest, *Proc. Natl. Acad. Sci.* **2013**, *110*, 3276.

[44] Z. Y. Wei, Z. V. Guo, L. Dudte, H. Y. Liang, L. Mahadevan, *Phys. Rev. Lett.* **2013**, *110*, 215501.

[45] K. C. Cheung, T. Tachi, S. Calisch, K. Miura, *Smart Mater. Struct.* **2014**, *23*, 094012.

[46] Y. Cho, J.-H. Shin, A. Costa, T. A. Kim, V. Kunin, J. Li, S. Y. Lee, S. Yang, H. N. Han, I.-S. Choi, D. J. Srolovitz, *Proc. Natl. Acad. Sci.* **2014**, *111*, 17390.

[47] D. M. Sussman, Y. Cho, T. Castle, X. Gong, E. Jung, S. Yang, R. D. Kamien, *Proc. Natl. Acad. Sci.* **2015**, *112*, 7449.

[48] S. Zhuo, S. Zhao, Z. Xie, Y. Hao, Y. Xu, T. Zhao, H. Li, E. M. Knubben, L. Wen, L. Jiang, M. Liu, *Sci. Adv.* **2020**, *6*, eaax1464.

[49] L. Du, W. Shi, H. Gao, H. Jia, Q. Zhang, M. Liu, Y. Xu, *Adv. Funct. Mater.* **2024**, *34*, 2314123.

[50] M. P. Bendsoe, O. Sigmund, *Topology Optimization: Theory, Methods, and Applications*, Springer, Berlin, Heidelberg **2013**.

[51] O. Sigmund, K. Maute, *Struct. Multidiscip. Optim.* **2013**, *48*, 1031.

[52] J. Pinskier, X. Wang, L. Liow, Y. Xie, P. Kumar, M. Langelaar, D. Howard, *Adv. Intell. Syst.* **2024**, *6*, 2300505.

[53] Hibbitt, Karlsson and Sorensen, "ABAQUS/Standard: User's manual," Hibbitt, Karlsson & Sorensen, **1997**.

[54] N. H. Kim, *Introduction to Nonlinear Finite Element Analysis*, Springer, New York **2014**.

[55] A. Pagoli, F. Chapelle, J. A. Corrales-Ramon, Y. Mezouar, Y. Lapusta, *Smart Mater. Struct.* **2021**, *31*, 013001.

[56] M. P. Bendsøe, O. Sigmund, *Arch. Appl. Mech.* **1999**, *69*, 635.

[57] K. Svanberg, *Int. J. Numer. Methods Eng.* **1987**, *24*, 359.

[58] R. T. Haftka, Z. Gürdal, *Elements of Structural Optimization*, Springer, Dordrecht **2012**.

[59] K. Deb, A. Pratap, S. Agarwal, T. Meyarivan, *IEEE Trans. Evol. Comput.* **2002**, *6*, 182.

[60] B. Kim, U. Jeong, B. B. Kang, K.-J. Cho, *IEEE-ASME Trans. Mechatron.* **2021**, *26*, 2932.

[61] S. Cheon, D. Kim, S. Kim, B. B. Kang, J. Lee, H. Gong, S. Jo, K. -J. Cho, J. Ahn, *IEEE Trans. Med. Robotics Bionics* **2020**, *3*, 179.

[62] C. Shentu, J. Burgner-Kahrs, *arXiv Preprint* **2024**, arXiv:2409.13165.

[63] M. M. Dalvand, S. Nahavandi, R. D. Howe, *IEEE Trans. Robot.* **2018**, *34*, 1215.